

# Tripling the Capacity of Optical Vortices by Nonlinear Metasurface

Zhi Li, Wenwei Liu, Zhancheng Li, Chengchun Tang, Hua Cheng, Junjie Li, Xianzhong Chen, Shuqi Chen,\* and Jianguo Tian

Optical vortices have emerged as a potential approach to enhance data capacity for its extra degree of freedom of orbital angular momentum. Although linear metasurfaces have been used to generate optical vortices, their capacity can be further increased by involving nonlinear frequency conversions, providing new channels for data storage. Here, by introducing second harmonic Pancharatnam–Berry phase, one linear and two second harmonic optical vortices with different topological charges focused into different focal lengths can be generated simultaneously from the proposed metasurface, which can store threefold optical vortices compared with the conventional linear geometric metasurfaces have been demonstrated. Besides, the 2D multifocal metalens with same strength for each focus emerged from the parabolic phase factor has been experimentally observed. This nonlinear optical vortex generation process represents a new strategy for enhancing the capacity of optical communications and multi-channels integrated optical communications.

propagation, which have been used to produce nearly arbitrary wavefront of electromagnetic wave at subwavelength scale.<sup>[1–3]</sup> Ultrathin planar metasurface devices can facilitate device miniaturization and system integration. Few-layer metasurfaces are also becoming an increasingly important line of research because of their emergent functionality and controllability.<sup>[4–6]</sup> Geometric metasurfaces are based on the Pancharatnam–Berry (P–B) phase change, which can transform the incident circularly polarized light into the opposite helicity with an imprinted geometric phase  $2\sigma\theta$ , where  $\sigma = \pm 1$  stands for the circular polarization state of the incident light and  $\theta$  is the in-plane orientation angle of each meta-atom.<sup>[7,8]</sup> Geometric metasurfaces have been applied to demonstrate exotic applications, including optical

## 1. Introduction

Recently, metasurfaces have attracted considerable interest due to their unprecedented capability in the manipulation of light

holography,<sup>[9–11]</sup> ultrathin flat metalenses,<sup>[12–14]</sup> and optical spin Hall effects.<sup>[15–18]</sup> Recently, this concept has been extended to nonlinear optical regime and the nonlinear P–B phase of metasurfaces was proved to be determined by both selection rules and the nonlinear P–B phase elements.<sup>[19,20]</sup> Based on the nonlinear phase control process, nonlinear optical spin-wavelength multiplexed holography<sup>[21]</sup> and nonlinear optical image encoding<sup>[22]</sup> have been demonstrated. In comparison with linear geometric metasurfaces, nonlinear geometric metasurfaces can store several-fold phase information due to the linear and nonlinear signals carrying different geometric phases.

Dr. Z. Li, Dr. W. Liu, Dr. Z. Li, Prof. H. Cheng, Prof. S. Chen, Prof. J. Tian  
The Key Laboratory of Weak Light Nonlinear Photonics  
Ministry of Education  
School of Physics and TEDA Institute of Applied Physics  
Nankai University  
Tianjin 300071, China  
E-mail: schen@nankai.edu.cn

Dr. C. Tang, Prof. J. Li  
Beijing National Laboratory for Condensed Matter Physics  
Institute of Physics  
Chinese Academy of Sciences  
P.O. Box 603, Beijing 100190, China

Prof. X. Chen  
Institute of Photonics and Quantum Sciences  
School of Engineering and Physical Sciences  
Heriot-Watt University  
Edinburgh EH14 4AS, UK

Prof. H. Cheng, Prof. S. Chen, Prof. J. Tian  
The collaborative Innovation Center of Extreme Optics  
Shanxi University  
Taiyuan, Shanxi 030006, China

The ORCID identification number(s) for the author(s) of this article can be found under <https://doi.org/10.1002/lpor.201800164>

DOI: 10.1002/lpor.201800164

An optical vortex has a helical phase front and doughnut-shaped spatial profile, referring to an optical beam carrying orbital angular momentum (OAM), is characterized by an azimuthal phase dependence  $\exp(i l \alpha)$ , where  $l$  being an integer is the topological charge of the beam and  $\alpha$  is the azimuthal angle.<sup>[23–25]</sup> OAM has an unbounded value of  $l\hbar$  per photon, which means the data capacity can be dramatically enhanced by OAM-carrying beam, thus the optical vortex has a promising prospect in modern optical communications.<sup>[26,27]</sup> The conventional optical vortex generation methods, such as spiral phase plates,<sup>[28]</sup> space light modulators,<sup>[29]</sup> and computer-generated holograms,<sup>[30]</sup> affect the compactness of optical systems and limit its applications in the field of nanotechnology. Recently, optical vortices,<sup>[31–34]</sup> focused optical vortices,<sup>[35,36]</sup> and a volumetric optical vortex array<sup>[37]</sup> have been generated based on geometric metasurfaces. However, these works only consider the linear signal of

the optical vortex, the potential of the optical vortex in enhancing data capacity can be explored further if nonlinear P–B phase is added as nonlinear geometric metasurfaces can store more phase information than their linear counterparts.

Here we propose and experimentally demonstrate by introducing second harmonic P–B phase, the metasurface can store threefold optical vortices with different topological charges compared with the conventional linear geometric metasurfaces. Besides, the optical vortices are designed to be focused for enhancing the weak signals of the second harmonic generation (SHG). Here we adopt the parabolic phase distribution for focusing instead of hyperbolic one since its mathematical linearity fits properly for multiplexing of linear and nonlinear P–B phases. As a result, one linear and two SHG optical vortices with different topological charges focused into different focal lengths can be generated simultaneously from the proposed single-layer metasurface. Utilizing this nonlinear optical vortices generation process can promise great applications in enhancing data capacity of optical communications and newer information security. Furthermore, we reveal the new phenomenon of parabolic phase distribution for focusing and observe 2D multifocal metalens in experiment.<sup>[38]</sup>

## 2. Results and Discussion

The plasmonic nonlinearity phase control can be generally divided into two processes, selection rules and nonlinear P–B phase elements. Different from the conventional selection rules of harmonic generation that are mainly based on the symmetries at the atomic level, plasmonic selection rules governing the plasmonic nonlinear processes can be imposed by the rotational symmetry of metasurfaces. It has been demonstrated that for a fundamental wave with circularly polarized state,  $\sigma$  that can excite a metasurface, the allowed orders  $n$  for harmonic generation are  $n = mj \pm 1$ , where  $j$  is an arbitrary integer,  $m \geq 3$  is the symmetry order of the metasurface and “ $\pm$ ” stands for the same or opposite circular polarization of harmonic generation. Due to the deep subwavelength thickness of metasurfaces, the selection rules can be extended to lower twofold and even onefold rotational symmetries.<sup>[19–21]</sup> For the allowed nonlinear signals, the nonlinear geometric phases  $(n - 1)\sigma\theta$  or  $(n + 1)\sigma\theta$  are introduced of the  $n$ th harmonic generation with the same or opposite circular polarization to that of the fundamental wave. The split ring resonators (SRRs) are selected as meta-atoms due to the lack of centrosymmetry and high SHG efficiency by exciting their magnetic-dipole resonances.<sup>[39,40]</sup> According to above analysis, for a fundamental wave with circularly polarized state  $\sigma$ , the non-centrosymmetric SRR with orientation angle  $\theta$  allows both SHG processes for the same ( $\sigma$ ) or opposite polarization state ( $-\sigma$ ) as the incident polarization and these two SHG signals with different spins  $\sigma$  and  $-\sigma$  acquire different nonlinear P–B phases of  $\sigma\theta$  and  $3\sigma\theta$ , respectively. Thus, by introducing SHG process, a metasurface can generate one linear ( $2\sigma\theta$ ) and two nonlinear ( $\sigma\theta$  and  $3\sigma\theta$ ) P–B phases, corresponding to the optical signals of different wavelengths and spins, noticeably, these different P–B phases are linear dependent since they arise from the same principle.

The hyperbolic phase distribution for focusing can be expressed as  $\varphi_0(r) = k_0\sqrt{r^2 + f_0^2}$ , where  $k_0$  is the linear wave

vector,  $r$  is the distance of each meta-atom from the coordinate origin, and  $f_0$  is the linear focal length. This formula can be rewritten as  $\varphi_n(r) = k_n\sqrt{r^2 + f_n^2}$  when  $n$ th harmonic generation signal is considered, where  $\varphi_n(r) = \frac{n\pm 1}{2}\varphi_0(r)$ ,  $k_n = nk_0$  is the nonlinear wave vector and  $f_n$  is the nonlinear focal length. Thus the relation between linear and nonlinear focusing formulae is  $(\frac{\varphi_n}{k_n})^2 = [\frac{(n\pm 1)}{2n}]^2(\frac{\varphi_0}{k_0})^2$ , the equation makes sense only if  $n = \pm 1$ , meaning that the nonlinear focal length does not have exact solutions. The parabolic phase distribution for focusing which has shown potential applications in non-paraxial plasmonic Fourier optics recently can be expressed as<sup>[41]</sup>

$$\varphi_0 = \frac{k_0 r^2}{2f_0} \quad (1)$$

The formula can be rewritten as  $\varphi_n = \frac{k_n r^2}{2f_n}$  for  $n$ th harmonic generation signal and the relation between linear and nonlinear focusing formulae is  $\frac{\varphi_n}{k_n} = \frac{n\pm 1}{2n} \frac{\varphi_0}{k_0} = \frac{r^2}{2f_n}$ . Thus, the nonlinear focal length is given by

$$f_n = \frac{2n}{n \pm 1} f_0 \quad (2)$$

Therefore, the transmitted SHG of spin  $\sigma$  and  $-\sigma$  have nonlinear focal lengths of  $4f_0$  and  $4f_0/3$ , respectively. In order to achieve the desired focusing optical vortices, the metasurface needs to incorporate two distinct phase profiles of a lens and a vortex plate. Normally, the phase distribution of the metasurface for both linear and nonlinear could be obtained as

$$\varphi = \begin{cases} \frac{kr^2}{2f} + l \cdot \arctan\left(\frac{y}{x}\right), & x > 0 \\ \frac{kr^2}{2f} + l \cdot \left[\pi + \arctan\left(\frac{y}{x}\right)\right], & x < 0 \end{cases} \quad (3)$$

where the parameter  $l$  represents the topological charge of the radiated OAM light, we set linear focal length  $f_0 = 30 \mu\text{m}$  and topological charge  $l_0 = 2$  in this paper. Based on the aforementioned analysis, one linear focusing optical vortex ( $-\sigma$ ) with  $f_0 = 30 \mu\text{m}$ ,  $l_0 = 2$ , and two nonlinear focusing optical vortices with  $f_{n1} = 120 \mu\text{m}$ ,  $l_{n1} = 1$  ( $\sigma$ ) and  $f_{n2} = 40 \mu\text{m}$ ,  $l_{n2} = 3$  ( $-\sigma$ ) can be generated simultaneously as shown in **Figure 1**. The insets show the numerical intensities and interference patterns of the optical vortices.

As a typical structure for investigating SHG process, SRRs have been proved to largely boost the SHG process by exciting the magnetic-dipole resonances.<sup>[39]</sup> Therefore, the magnetic-dipole mode of SRRs is designed to fit the wavelength of illumination around 1550 nm. In our study, all numerical simulations were performed using the finite-difference time-domain (FDTD) method. The complex dielectric constants of gold and silica substrate were taken from measured data.<sup>[42]</sup> For the theoretical simulations, the meta-atom has periodic boundary conditions in the  $x$ - and  $y$ -directions, light is illuminated from the substrate side and perfectly matched layers are used at the bottom of the air domain. The single gold SRR is characterized by four geometrical parameters: length of long arm  $L_x$ , length of short arm  $L_y$ , width  $w$ , and thickness  $h$  of the antenna. The period between the antennas is 400 nm in both directions. **Figure 2a** shows the simulated

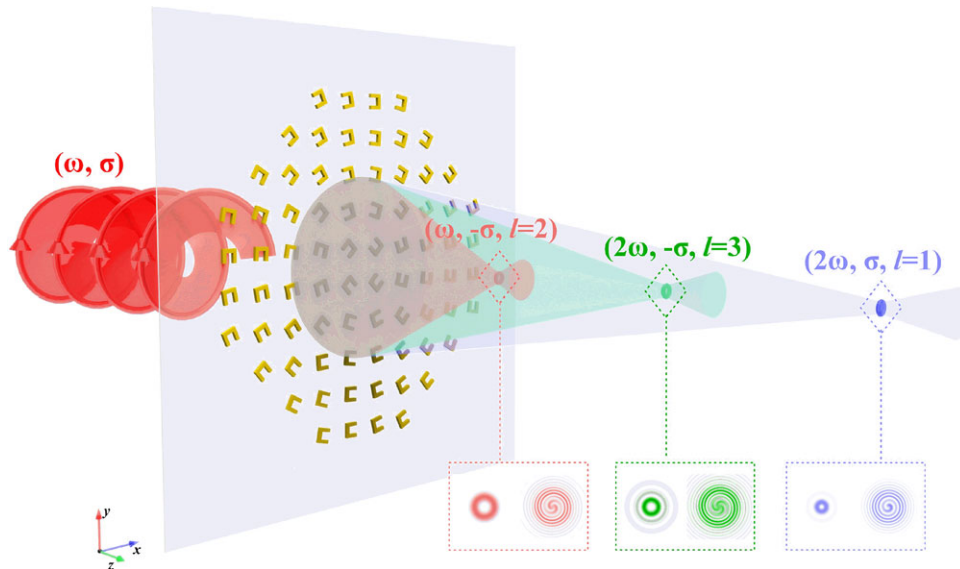


**Figure 1.** Schematic of focusing optical vortices with proposed metasurface. With different combination of spin and wavelength, the three optical vortices with different topological charges focused at different focal planes. The insets show the numerical intensities and interference patterns of the optical vortices.

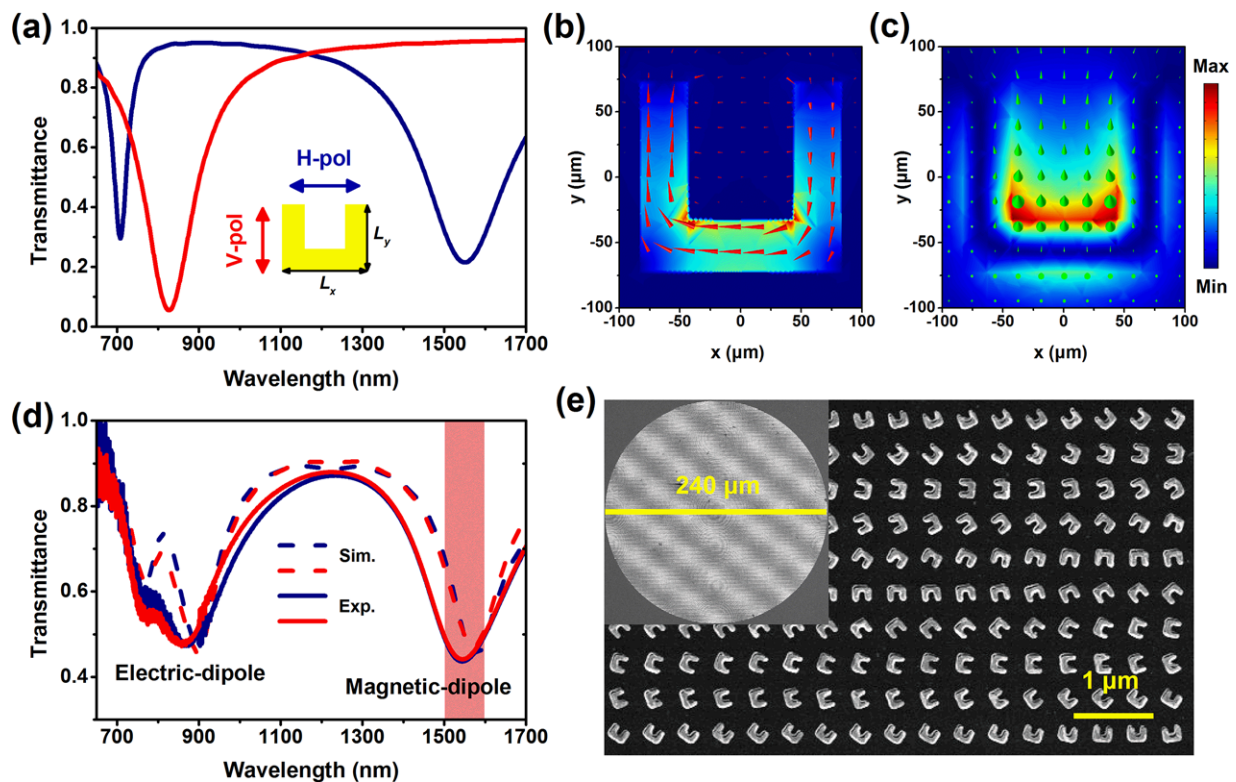


**Figure 2.** Properties of the fabricated metasurface. a) Simulated transmission spectra for horizontal and vertical polarized incident light of uniformly arranged SRRs. Length of long arm  $L_x$ , short arm  $L_y$ , width  $w$ , and thickness  $h$  of the nanoantenna are 167, 145, 40, and 35 nm, respectively. Characteristic snapshots of b) current density  $\mathbf{J}$  and c) magnetic field  $\mathbf{B}$  of an SRR at wavelength of 1550 nm. The scale bar is adapted for each figure. d) Simulated (dashed lines) and measured (solid lines) transmission spectra for horizontal and vertical polarized incident light of the fabricated metasurface for focusing optical vortices. The incident wavelengths are marked by a red stripe. e) SEM micrograph of a part of the fabricated metasurface. The set shows the whole metasurface with a radius of 120  $\mu\text{m}$ .

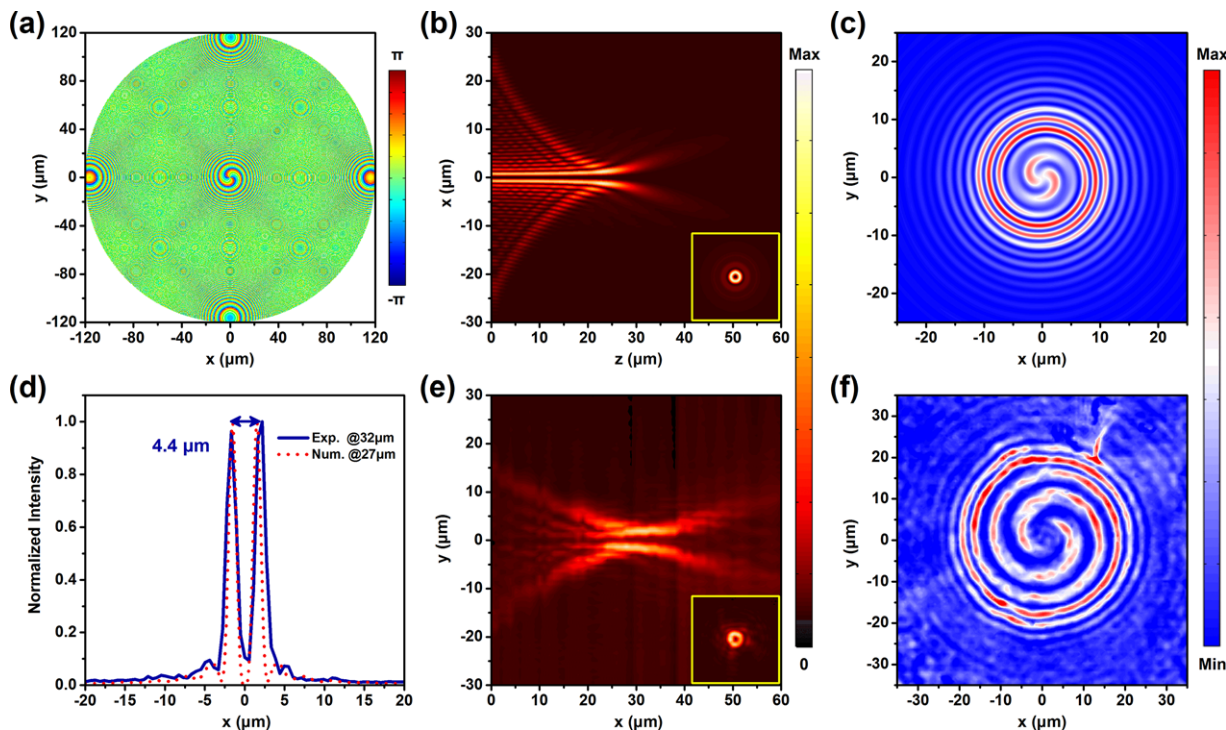


**Figure 3.** Experimental demonstration of the linear focusing optical vortex. a) Calculated phase profile for linear focusing optical vortex with spin  $-\sigma$ . b) Numerical and e) measured intensity distributions along the propagation direction, the insets show the intensity distributions at focal planes. The scale bar is adapted for each figure. c) Numerical and f) measured interference patterns of the focusing optical vortices. The scale bar is adapted for each figure. d) The numerical and measured intensity cross profiles of the focusing optical vortices at focal planes.

transmission spectra of uniformly arranged SRRs for horizontal (solid blue line) and vertical (solid red line) polarized incident light, the magnetic-dipole mode located at 1550 nm can be excited by horizontal polarized component and the electric-dipole mode located around 800 nm. Due to the existence of toroidal current, strong magnetic-dipole resonance in the range of fundamental wavelengths has been excited as shown in Figure 2b,c. To experimentally verify the nonlinear optical vortices design, a metasurface consisting of gold SRRs was fabricated using electron beam lithography (EBL), the simulated (dashed lines) and measured (solid lines) linear transmission spectra of the nonlinear optical vortices generation metasurface are displayed in Figure 2d, and Figure 2e shows the scanning electron microscopy (SEM) image of a small area across the fabricated metasurface and the inset shows the whole metasurface with a radius of 120 μm. The principle of the orientation angle for each SRR antenna is based on Equation (3), which combines a lens factor and a vortex plate. As expected before, the metasurface has a magnetic-dipole mode at 1530 nm for both horizontal and vertical polarizations, which is slightly blue shifted compared with the designed result. The distribution of the orientation angles among SRRs of the optical vortex component is isotropic in both horizontal and vertical directions, and the lens component can be seen as nearly isotropic in each radiated direction. Thus the final distribution of the orientation angles of the SRRs across the whole metasurface is nearly isotropic, the two polarized transmission spectra are identical and higher than the simulated spectra of uniformly arranged SRRs due to the average effect of two polarization directions.

We first demonstrated the evolution of the linear focusing optical vortex with topological charge  $l_0 = 2$  and focal length  $f_0 = 30 \mu\text{m}$ . A home-built microscope was used for measuring both linear and nonlinear radiated electric field intensities (see Figure S1, Supporting Information). The combination of the vortex plate and lens factor results in a pair of spirals of the phase distribution as shown in Figure 3a. As presented in Figure 3b, numerical intensity distribution along the propagation direction reveals that the optical vortex concentrate while propagating with a focal length of 27 μm. The inset indicates the intensity distribution at the focal plane, which has a doughnut-shaped spatial profile with characteristic intensity minimum at the center, further confirming a focused optical vortex. Under LCP ( $\sigma$ ) illumination, the focusing optical vortex has an opposite spin ( $-\sigma$ ) to that of the incident beam, thus a quarter-wave plate (QWP) and a linear polarizer (LP) were placed in front of the camera to filter out any co-polarized light. The experimental results are presented in Figure 3e with a measured focal length about 32 μm, which generally agrees with the designed value and the inset indicates the measured intensity distribution at the focal plane. The intensity cross profiles depict that both numerical (red dashed line) and measured (blue solid line) center-to-center distances of the doughnut-shaped spatial profile at the focal plane are less than 5 μm as shown in Figure 3d, which can be readily integrated into micro-optical platforms due to its compact dimension. To verify the topological charge of the focusing optical vortex, partial transmitted co-polarized light was deliberately reserved by turning the LP, thus it could interfere with the focusing optical vortex as a

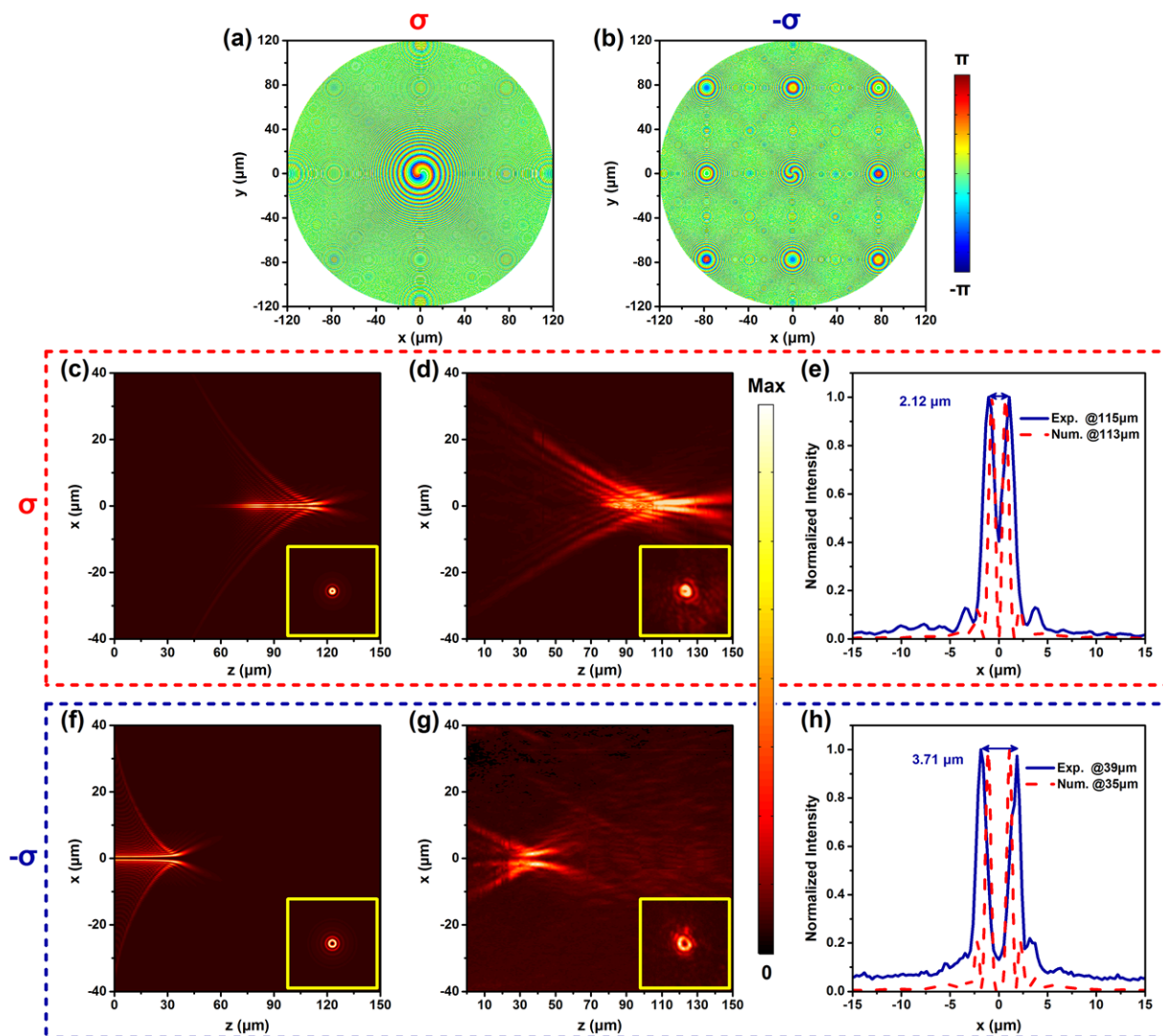


**Figure 4.** Experimental demonstration of the SHG focusing optical vortex. Calculated phase profile for nonlinear focusing optical vortex with spin a)  $\sigma$  and b)  $-\sigma$ . Numerical intensity distributions along the propagation direction with spin c)  $\sigma$  and f)  $-\sigma$ , the insets show the intensity distributions at focal planes. Measured intensity distributions along the propagation direction with spin d)  $\sigma$  and g)  $-\sigma$ , the insets show the intensity distributions at focal planes. The numerical and measured intensity cross profiles of the focusing optical vortices at focal planes with spin e)  $\sigma$  and h)  $-\sigma$ . The scale bar is adapted for each figure.

reference wave. The intensity of the interference pattern can be manifested by rotating petals encircling the beam centers, where the value and sign of topological charge  $l$  are determined by the number and twisting direction of these petals and from both numerical (Figure 3c) and experimental (Figure 3f) results, the two petals unambiguously validate  $l_0 = 2$ .

We next measured the spin-dependent nonlinear focusing optical vortices at SHG wavelength. The nonlinear focusing optical vortices with same ( $\sigma$ ) or opposite ( $-\sigma$ ) circular polarization to that of the fundamental wave can be selectively demonstrated by turning a QWP and an LP placed in front of the camera. For the focusing optical vortex with the same spin to the illumination light, the theoretical phase distribution is depicted in Figure 4a, different from the linear one, only one spiral emerges. The numerical (Figure 4c) and measured (Figure 4d) intensity profiles

along the propagation direction both indicate a nonlinear focal length  $f_{n1}$  about  $115 \mu\text{m}$ , which accords with the theoretical analysis of Equation (2). The intensity cross profiles at the focal plane, as shown in Figure 4e, indicate that the diameter of the nonlinear annular ring is about  $2 \mu\text{m}$  for both numerical and measured results due to the smaller topological charge and shorter wavelength compared with the linear one, this phenomenon can also be observed through the intensity distribution (inset of Figure 4d). For the focusing optical vortex with the opposite spin to the illumination light, the theoretical phase distribution appears as three spirals as depicted in Figure 4b, the numerical (Figure 4f) and measured (Figure 4g) nonlinear focal lengths  $f_{n2}$  are both about  $39 \mu\text{m}$ . The diameter of the nonlinear annular ring is less than  $4 \mu\text{m}$  at the focal plane as shown in Figure 4h. Besides, this nonlinear optical vortices method has sufficient less noise than

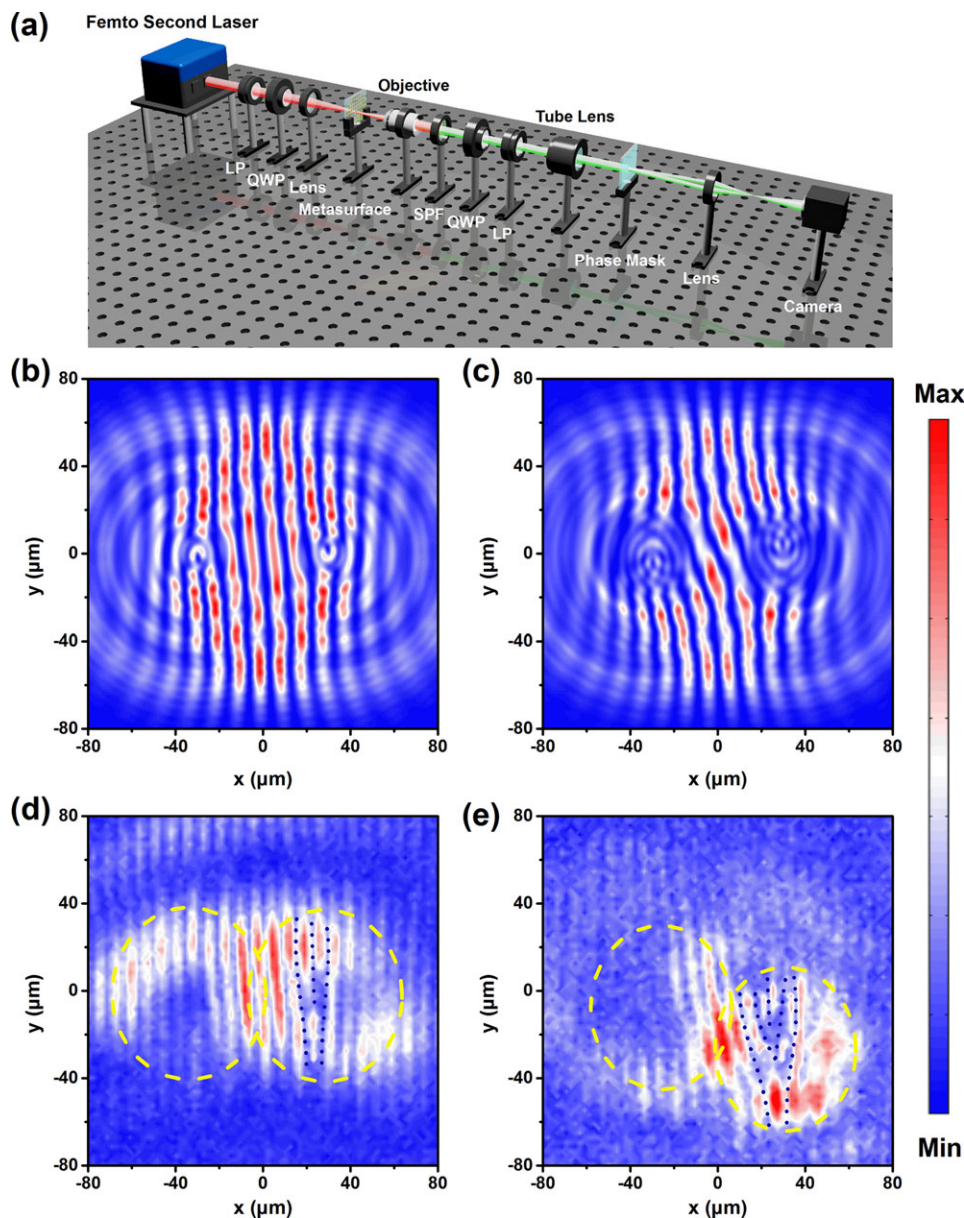


**Figure 5.** Experimental measurement of the topological charges of SHG optical vortices. a) Illustration of the measurement set-up for measuring the topological charges of SHG optical vortices. LP, linear polarizer; QWP, quarter-wave plate; SPF, short-pass filter. Numerical self-interference patterns of the SHG optical vortices with spin b)  $\sigma$  and c)  $-\sigma$ . Measured self-interference patterns of the SHG optical vortices with spin d)  $\sigma$  and e)  $-\sigma$  after the phase mask plane. The number of branches reveals that the SHG beams possess OAM of  $l_{n1} = 1$  and  $l_{n2} = 3$ , respectively. The scale bar is adapted for each figure.

the purely linear way since each spin-wavelength combination, all meta-atoms provide effective phase. Furthermore, since no background noise derived from the illumination light for nonlinear focusing optical vortices, a larger signal-to-noise ratio can be obtained at SHG wavelength range.

How to quantify the topological charges of optical vortices for ultrafast laser beams is usually a challenging problem since it is hard for conventional interferometry to satisfy the ultrashort coherence length from two arms. Recently, a new methodology has been demonstrated to measure the topological charges of nonlinear optical vortices through on-chip metasurface interferometry;

however, this approach can only be applied for specific designed metasurfaces.<sup>[43]</sup> To overcome this constraint, we proposed a simplified interferometry by using  $\pm 1$  order phase mask, which can highly suppress zero order and diffract light equally and maximally into the  $\pm 1$  orders as shown in Figure 5a. Self-interference between these two orders creates an interference pattern with half period of the phase mask, thus a pair of dislocations in the fringe pattern can appear in the interferogram for the optical vortex. As shown in both numerical (Figure 5b,c) and measured (Figure 5d,e) results, one branch ( $\sigma$ ) and three branches ( $-\sigma$ ) have additionally appeared in the fringe patterns, confirming the

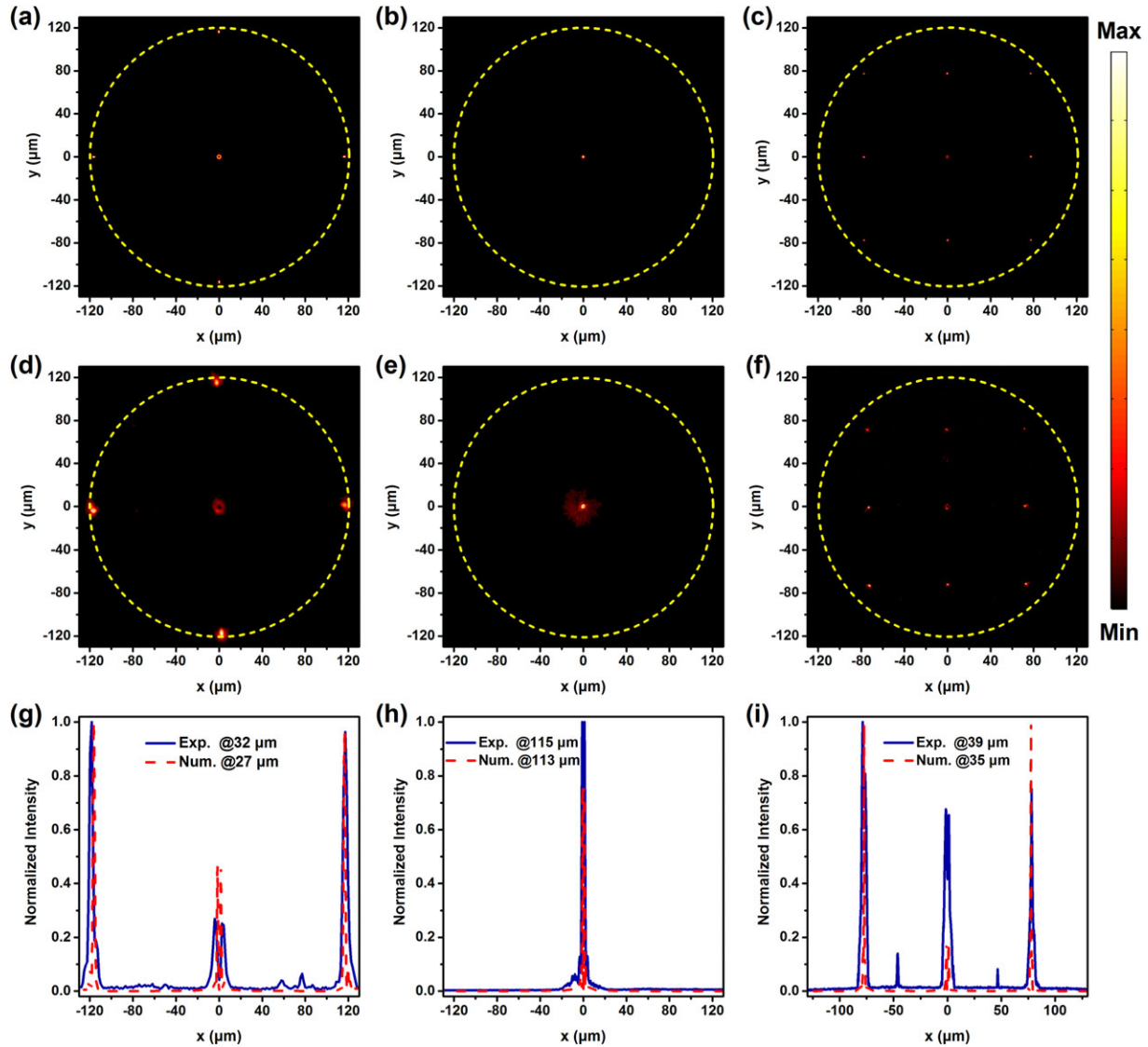


**Figure 6.** Observation of multifocal lenses. Numerical intensity distributions at focal planes of the linear focusing optical vortices with spin a)  $-\sigma$ , and SHG focusing optical vortices with spin b)  $\sigma$  and c)  $-\sigma$ . Measured intensity distributions at focal planes of the linear focusing optical vortices with spin d)  $-\sigma$ , and SHG focusing optical vortices with spin e)  $\sigma$  and f)  $-\sigma$ . The scale bar is adapted for each figure. The numerical and measured intensity cross profiles of the linear focusing optical vortex with spin g)  $\sigma$  and SHG focusing optical vortices with spin h)  $\sigma$  and i)  $-\sigma$  at focal planes.

presence of phase defects at the cores of these two SHG beams, and the number of branches ensures that the SHG optical vortices carry topological charges of  $l_{n1} = 1$  and  $l_{n2} = 3$ , respectively.

A parabolic phase profile can be seen as the first order approximation of Taylor expansion of a hyperbolic phase distribution, thus it is commonly used to simplify the design of a metalens with small numerical aperture.<sup>[44]</sup> However, recent research has proved that a multifocal metalens can be achieved based on the parabolic phase profile if the metalens is large enough.<sup>[38]</sup> Here, we have experimentally observed the 2D multifocal metalens since the lens factor of the focusing optical vortices is adopted as the parabolic phase profile. The normalized 2D phase profiles of discrete meta-atoms of the linear focusing optical vortex with spin  $-\sigma$ , SHG focusing optical vortices with spin  $\sigma$  and  $-\sigma$  are shown in Figures 3a, 4a,d, respectively, and these aperiodic

phase profiles, interestingly, can generate periodic focusing profiles. The phase difference  $\Delta\varphi_i$  between two adjacent meta-atoms varies periodically from  $-\pi$  to  $\pi$ , which cannot be considered close to a constant. The foci can periodically appear as long as the metasurface is large enough. The minimum period of the foci can be expressed as

$$D = \frac{\lambda f}{\Lambda} \quad (4)$$

where  $\Lambda$  is the period of each meta-atom. According to Equation (4), the theoretical distances between the foci of linear with spin  $-\sigma$ , SHG with spin  $\sigma$  and  $-\sigma$  focusing optical vortices are 116, 234, and 78  $\mu\text{m}$ , respectively, and the numerical (Figure 6a–c) and measured (Figure 6d–f) results are in agreement with the

theoretical ones. Besides, the intensity cross profiles of both numerical (red dashed line) and measured (blue solid line) intensities depict that the intensity of each focus is equal as shown in Figure 6g–i, thus the metalens can serve as a generalized grating with the same strength for all the diffracting orders.

### 3. Conclusions and Outlook

In conclusion, we have proposed and demonstrated that by introducing nonlinear geometric phases, threefold capacity of optical vortices can be achieved using an ultrathin nonlinear metasurface with sufficient low noise compared with the conventional linear geometric ones. One linear and two SHG optical vortices with different topological charges focused into different focal lengths can be generated simultaneously, each focusing optical vortex can only be read out by specific combination of spin and wavelength. Besides, the 2D multifocal metalenses for both linear and nonlinear regimes have also been observed based on the parabolic phase factor. Although the efficiency of the nonlinear metasurface is low in our experiment compared with the linear metasurfaces which have been used to manipulate the angular momentum of light<sup>[18,34]</sup> since the centrosymmetric atomic lattice of noble metals forbids the SHG in the bulk noble metals, the SHG process can provide more information channels and can be further enhanced by adopting hybrid or semiconductor-based metasurfaces.<sup>[45,46]</sup> The nonlinear focusing optical vortices can open new avenues for high-capacity OAM communications, multi-channel optical manipulation and information encryption. We note that the capacity can be further extended by this methodology by introducing other nonlinear processes such as third harmonic generation (THG), (see Figure S2, Supporting Information), combining with multitasking or volumetric generation processes.

### 4. Experimental Section

**Sample Fabrication:** The sample was prepared using a standard EBL and a lift-off process. First, a layer of poly(methyl methacrylate), (PMMA) with thickness of 120 nm which is an empirical value and a layer of poly(3,4-ethylenedioxythiophene) poly(styrene sulfonate) (PEDOT:PSS) with thickness of 35 nm were spun coated on the fused silica substrate by sequence. The PEDOT:PSS layer was intended for charge release during the EBL process by employing a 100 kV voltage, 200 pA current, and 1000  $\mu\text{C cm}^{-2}$  dose. After defining the nanometer scale metasurface patterns by the EBL process, the PEDOT:PSS layer was removed with pure water for 60 s and PMMA was developed with methyl isobutyl ketone (MIBK)/isopropyl alcohol (IPA) (3:1) for 40 s. Then a 2 nm Cr layer and a 35 nm Au layer were deposited on the resist by sequence with electron beam evaporation deposition (EBD) method. Then the Cr film was striped by removing PMMA with hot acetone at a temperature of 60 °C for 20 min, leaving the metal pattern on substrate. The Cr layer here aimed to enhance adhesion between the silica surface and the gold layer.

**Measurement Procedure:** An Erbium-doped ultrafast fiber laser (Toptica Photonics AG FemtoFiber Pro NIR, repetition frequency: 80 MHz, pulse length:  $\approx 80$  fs) centered at 1550 nm was coupled to a home-built microscopy. An LP and a QWP were combined to generate the incident circularly polarized light, the metasurface was illuminated at normal incidence and the generated linear and nonlinear optical vortices were filtered by another combination of a QWP and an LP, then collected with an objective, a tube lens, and a scientific camera. The objective, tube lens

(Thorlabs ITL200), and camera were all integrated on a XYZ translation stage to scan the focusing profiles of the optical vortices with a step of 1  $\mu\text{m}$  along z-direction. For linear measurement, an average power of 1 mW, a 50 $\times$  objective (SIGMA-KOKI PAL-50-NIR-HR-LC00 50  $\times$  NA = 0.67), and an InGaAs camera (HAMAMATSU InGaAs C10633) were used, the lens and short-pass filters were removed. For nonlinear measurement, the fundamental pulses had an average power of 350 mW and were focused to a spot with a diameter of  $\approx 200$   $\mu\text{m}$  (by a lens with focal length of 150 mm), which corresponded to a peak intensity of 0.17 GW  $\text{cm}^{-2}$ . A 20 $\times$  objective (SIGMA-KOKI PAL-20-NIR-HR-LC00 20  $\times$  NA = 0.45) and an sCMOS camera (HAMAMATSU ORCA-Flash4.0 V3) were used for collecting the SHG signals. For measurement of topological charges of SHG optical vortices, a  $\pm 1$  order phase mask (made of JGS1, with period of 18  $\mu\text{m}$ , depth of 0.87  $\mu\text{m}$ ) was placed behind the tube lens, and a lens (with focal length of 75 mm) was used to magnify the images.

### Supporting Information

Supporting Information is available from the Wiley Online Library or from the author.

### Acknowledgements

This work was supported by the National Key Research and Development Program of China (2016YFA0301102 and 2017YFA0303800), the Ministry of Science and Technology of China (2016YFA0200803 and 2016YFA0200402), the Natural Science Foundation of China (11774186 and 11574163), the Natural Science Foundation of Tianjin (16JCQNJC01700), and 111 Project (B07013).

### Conflict of Interest

The authors declare no conflict of interest.

### Keywords

metasurfaces, optical vortex, Pancharatnam–Berry phase, second harmonic generation

Received: June 13, 2018

Revised: August 29, 2018

Published online:

- [1] A. V. Kildishev, A. Boltasseva, V. M. Shalaev, *Science* **2013**, *339*, 1232009.
- [2] N. Meinzer, W. L. Barnes, I. R. Hooper, *Nat. Photonics* **2014**, *8*, 889.
- [3] N. Yu, F. Capasso, *Nat. Mater.* **2014**, *13*, 139.
- [4] H. Cheng, Z. Liu, S. Chen, J. Tian, *Adv. Mater.* **2015**, *27*, 5410.
- [5] J. Li, S. Chen, H. Yang, J. Li, P. Yu, H. Cheng, C. Gu, H.-T. Chen, J. Tian, *Adv. Funct. Mater.* **2015**, *25*, 704.
- [6] J. Liu, Z. Li, W. Liu, H. Cheng, S. Chen, J. Tian, *Adv. Opt. Mater.* **2016**, *4*, 2028.
- [7] S. Pancharatnam, *Proc. Indian Acad. Sci. Sec. A* **1956**, *44*, 398.
- [8] M. V. Berry, *Proc. R. Soc. London, Ser. A* **1984**, *392*, 45.
- [9] L. Huang, X. Chen, H. Mühlenbernd, H. Zhang, S. Chen, B. Bai, Q. Tan, G. Jin, K.-W. Cheah, C.-W. Qiu, J. Li, T. Zentgraf, S. Zhang, *Nat. Commun.* **2013**, *4*, 2808.
- [10] L. Huang, H. Mühlenbernd, X. Li, X. Song, B. Bai, Y. Wang, T. Zentgraf, *Adv. Mater.* **2015**, *27*, 6444.

- [11] G. Zheng, H. Mühlenbernd, M. Kenney, G. Li, T. Zentgraf, S. Zhang, *Nat. Nanotech.* **2015**, *10*, 308.
- [12] X. Chen, L. Huang, H. Mühlenbernd, G. Li, B. Bai, Q. Tan, G. Jin, C.-W. Qiu, S. Zhang, T. Zentgraf, *Nat. Commun.* **2012**, *3*, 1198.
- [13] F. Aieta, P. Genevet, M. A. Kats, N. Yu, R. Blanchard, Z. Gaburro, F. Capasso, *Nano Lett.* **2012**, *12*, 4932.
- [14] M. Khorasaninejad, W. T. Chen, R. C. Devlin, J. Oh, A. Y. Zhu, F. Capasso, *Science* **2016**, *352*, 1190.
- [15] X. Yin, Z. Ye, J. Rho, Y. Wang, X. Zhang, *Science* **2013**, *339*, 1405.
- [16] M. Khorasaninejad, K. B. Crozier, *Nat. Commun.* **2014**, *5*, 5386.
- [17] Z. Li, W. Liu, H. Cheng, S. Chen, J. Tian, *Adv. Opt. Mater.* **2017**, *5*, 1700413.
- [18] X. Ling, X. Zhou, X. Yi, W. Shu, Y. Liu, S. Chen, H. Lou, S. Wen, D. Fan, *Light: Sci. Appl.* **2015**, *4*, e290.
- [19] S. Chen, G. Li, F. Zeuner, W. H. Wong, E. Y. B. Pun, T. Zentgraf, K. W. Cheah, S. Zhang, *Phys. Rev. Lett.* **2014**, *113*, 033901.
- [20] G. Li, S. Chen, N. Pholchai, B. Reineke, P. W. H. Wong, E. Y. B. Pun, K. W. Cheah, T. Zentgraf, S. Zhang, *Nat. Mater.* **2015**, *14*, 607.
- [21] W. Ye, F. Zeuner, X. Li, B. Reineke, S. He, C.-W. Qiu, J. Liu, S. Zhang, T. Zentgraf, *Nat. Commun.* **2016**, *7*, 11930.
- [22] F. Walter, G. Li, C. Meier, S. Zhang, T. Zentgraf, *Nano Lett.* **2017**, *17*, 3171.
- [23] G. Molina-Terriza, J. P. Torres, L. Torner, *Nat. Phys.* **2007**, *3*, 305.
- [24] A. M. Yao, M. J. Padgett, *Adv. Opt. Photon.* **2011**, *3*, 161.
- [25] L. Allen, M. W. Beijersbergen, R. J. C. Spreeuw, J. P. Woerdman, *Phys. Rev. A* **1992**, *45*, 8185.
- [26] J. Wang, J.-Y. Yang, I. M. Fazal, N. Ahmed, Y. Yan, H. Huang, Y. Ren, Y. Yue, S. Dolinar, M. Tur, A. E. Willner, *Nat. Photonics* **2012**, *6*, 488.
- [27] A. E. Willner, H. Huang, Y. Yan, Y. Ren, N. Ahmed, G. Xie, C. Bao, L. Li, Y. Cao, Z. Zhao, J. Wang, M. P. J. Lavery, M. Tur, S. Ramachandran, A. F. Molisch, N. Ashrafi, S. Ashrafi, *Adv. Opt. Photon.* **2015**, *7*, 66.
- [28] M. W. Beijersbergen, R. P. C. Coerwinkel, M. Kristensen, J. P. Woerdman, *Opt. Commun.* **1994**, *112*, 321.
- [29] J. E. Curtis, B. A. Koss, D. G. Grier, *Opt. Commun.* **2002**, *207*, 169.
- [30] N. R. Heckenberg, R. McDuff, C. P. Smith, A. G. White, *Opt. Lett.* **1992**, *17*, 221.
- [31] L. Huang, X. Chen, H. Mühlenbernd, G. Li, B. Bai, Q. Tan, G. Jin, T. Zentgraf, S. Zhang, *Nano Lett.* **2012**, *12*, 5750.
- [32] E. Karimi, S. A. Schulz, I. De Leon, H. Qassim, J. Upham, R. W. Boyd, *Light: Sci. Appl.* **2014**, *3*, e167.
- [33] E. Maguid, I. Yulevich, D. Veksler, V. Kleiner, M. L. Brongersma, E. Hasman, *Science* **2016**, *352*, 1202.
- [34] X. Yi, X. Ling, Z. Zhang, Y. Li, X. Zhou, Y. Liu, S. Chen, H. Luo, S. Wen, *Opt. Express* **2014**, *22*, 17207.
- [35] X. Ma, M. Pu, X. Li, C. Huang, Y. Wang, W. Pan, B. Zhao, J. Cui, C. Wang, Z. Zhao, X. Luo, *Sci. Rep.* **2015**, *5*, 10365.
- [36] M. Q. Mehmood, S. Mei, S. Hussain, K. Huang, S. Y. Siew, L. Zhang, T. Zhang, X. Ling, H. Liu, J. Teng, A. Danner, S. Zhang, C.-W. Qiu, *Adv. Mater.* **2016**, *28*, 2533.
- [37] L. Huang, X. Song, B. Reineke, T. Li, X. Li, J. Liu, S. Zhang, Y. Wang, T. Zentgraf, *ACS Photonics* **2017**, *4*, 338.
- [38] W. Liu, Z. Li, H. Cheng, S. Chen, J. Tian, *Phys. Rev. Applied* **2017**, *8*, 014012.
- [39] M. W. Klein, C. Enkrich, M. Wegener, S. Linden, *Science* **2006**, *313*, 502.
- [40] K. O'Brien, H. Suchowski, J. Rho, A. Salandrino, B. Kante, X. Yin, X. Zhang, *Nat. Mater.* **2015**, *14*, 379.
- [41] W. Liu, Z. Li, H. Cheng, C. Tang, J. Li, S. Zhang, S. Chen, J. Tian, *Adv. Mater.* **2018**, *30*, 1706368.
- [42] E. D. Palik, *Handbooks of Optical Constants of Solids*, Academic Press, New York **1998**.
- [43] G. Li, L. Wu, K. F. Li, S. Chen, C. Schlickriede, Z. Xu, S. Huang, W. Li, Y. Liu, E. Y. B. Pun, T. Zentgraf, K. W. Cheah, Y. Luo, S. Zhang, *Nano Lett.* **2017**, *17*, 7974.
- [44] H.-S. Ee, R. Agarwal, *Nano Lett.* **2016**, *16*, 2818.
- [45] Z. Li, W. Liu, Z. Li, H. Cheng, S. Chen, J. Tian, *Opt. Lett.* **2017**, *42*, 3117.
- [46] J. Lee, M. Tymchenko, C. Argyropoulos, P.-Y. Chen, F. Lu, F. Demmerle, G. Boehm, M.-C. Amann, A. Alù, M. A. Belkin, *Nature* **2014**, *511*, 65.